Article | Received 11 April 2025; Accepted 18 June 2025; Published 26 June 2025
https://doi.org/10.55092/am20250008

Preparation and characterization of copper parts printed by electrochemical additive manufacturing process

Xin Li, Wangping Wu* and Yu-ao An

Electrochemistry and Corrosion Laboratory, School of Mechanical Engineering and Rail Transit, Changzhou University, Changzhou 213164, China

* Correspondence author: wuwping@cczu.edu.cn.

Highlights:

- Cu parts Cu parts with various shapes were fabricated an ECAM technique.
- Effects of printing processes on morphology of copper parts were systematically studied.
- Optimal parameters of Cu lines were obtained by experiment and COMSOL simulation.

Abstract: This study presents the development and optimization of an electrochemical additive manufacturing technique for the fabrication of copper parts with various geometries, including dots, lines, and complex shapes, on metallic substrates. A customized syringe-based printing system was designed to enable precise, localized electrochemical additive manufacturing. The influences of key process parameters, including deposition voltage, nozzle feed rate, nozzle-to-substrate distance, and inter-electrode gap, on the deposition rate, surface morphology, and microstructure of the copper parts were systematically investigated. The results indicate that increasing the deposition voltage accelerates the growth rate but compromises surface smoothness and crystalline refinement. Optimal printing deposition was achieved at an applied voltage of 3 V, a nozzle feed rate of 0.4 mm/s, a nozzle-to-substrate distance of 0.1 mm, and the electrode spacing of 0.3 mm, yielding dense and uniform copper structures, as confirmed by optical microscopy and surface profilometry. The study highlights how variations in process parameters influence the deposition speed, surface quality, and microstructure of copper parts, establishing an optimal range for process settings. These findings offer significant guidance for achieving high-performance metal additive manufacturing in the future.

Keywords: electrochemical additive manufacturing; Copper; process parameter

1. Introduction

The continuous evolution of modern manufacturing technologies has significantly increased the demand for precise, efficient, and customizable fabrication methods. Additive manufacturing (AM) has emerged as a key solution, particularly for fabricating complex and miniaturized structures with high material utilization and reduced waste. Among various AM techniques, electrochemical additive manufacturing (ECAM) has attracted growing interest as a low-cost, environmentally friendly method

capable of producing microscale metal structures via localized electrochemical deposition [1–3]. Unlike conventional 3D printing methods such as direct metal laser sintering (DMLS), selective laser melting (SLM), or electron beam melting (EBM), ECAM does not require high-energy heat sources or vacuum environments. As a result, it avoids common issues such as thermal-induced warping, composition inhomogeneity, and high equipment costs.

Recent studies have demonstrated the feasibility of using ECAM to fabricate metallic microparts, such as copper [2], nickel [3], and platinum [4]. For example, Hu *et al*. [4] successfully printed integrated 3D interconnects using pure copper and platinum. ECAM's ability to leverage atomic-scale electrochemical control enables the formation of micro/nano features with excellent surface quality and dimensional accuracy. In addition, ECAM is compatible with a wide range of materials—including metals, alloys, and conductive polymers—making it highly suitable for applications in microelectronics, MEMS, and rapid prototyping. Efforts to improve its throughput by employing multicapillary systems have also shown promising results [5]. Despite these advantages, ECAM remains in its early developmental stages. Its build rate and part size are still limited compared to conventional high-throughput additive manufacturing (AM) methods. Moreover, the quality of ECAM-fabricated parts is highly sensitive to process parameters, and improper control may lead to defects such as poor surface morphology or residual stress [6,7]. To overcome these challenges, researchers have investigated the effects of individual parameters on ECAM performance. Several studies have systematically explored key influencing factors, including nozzle geometry [8], deposition voltage [9], electrode spacing [10], and additive synergy [11], all contributing to improved deposition uniformity, growth control, and microstructural stability of the printed parts. However, most of these investigations focused on isolated parameters or relied heavily on simulations [12,13], without experimentally addressing their combined effects. In parallel, a growing body of work has demonstrated the successful fabrication of complex three-dimensional (3D) metal structures using ECAM, with feature sizes ranging from the microscale to the sub-microscale. Sakairi *et al*. [14] developed a co-axial dual capillary droplet system to enable localized deposition of intricate copper microstructures. Chen *et al*. [15] proposed a low-cost desktop ECAM printer capable of producing metallic features at sub-millimeter resolution. Seol *et al*. [16] achieved internal architecture control in 3D metallic microstructures via electrodeposition-based 3D Printing. To further enhance resolution, Daryadel *et al*. [17] introduced pulsed localized 3D electrochemical printing process for nanotwinned nanostructures. Hengsteler *et al*. [18] reported ECAM printing into the sub-100 nm regime, demonstrating nanoscale manufacturing potential. Additionally, Liu *et al*. [19] integrated microfluidic technology for mesoscale ECAM printing, balancing resolution and throughput. Together, these advances validate ECAM's versatility across different scales and highlight its emerging role in precision manufacturing, microelectronics, and nanotechnology.

Copper is widely used in electronics, thermal management, and interconnect applications due to its excellent electrical and thermal conductivity. However, conventional fabrication techniques such as casting or subtractive machining often result in high material waste and poor resolution, particularly at the microscale [20,21]. ECAM offers a promising alternative for direct, high-resolution copper deposition with minimal waste, lower cost, and improved precision. In this study, a customized syringe based ECAM platform was constructed to fabricate copper microparts with various geometries, such as dots, lines, and complex patterns, on the substrates through ECAM process. A series of controlled experiments were conducted to systematically study the effects of key process parameters, including

deposition voltage, nozzle feed rate, nozzle-to-substrate distance, and electrode spacing, on the deposition rate, surface morphology, and microstructure of copper deposits by ECAM process. The results provide insights into the interplay between printing conditions and deposition quality, and define an optimal parameter window for achieving dense, uniform, and high-performance copper microparts.

2. Experimental

2.1. Electrochemical additive manufacturing platform

The electrochemical additive manufacturing process used in this work is based on localized meniscus-confined electrochemical deposition. A syringe-based nozzle delivers the electrolyte to the substrate surface, where copper ions are reduced under an applied voltage. This method allows controlled material growth in a confined region. The basic principles follow prior work on localized electrochemical printing [10]. In the present study, an electrochemical additive manufacturing apparatus was developed, leveraging a modified desktop 3D printer platform equipped with a precise X, Y, and Z three-axis linkage system to control the movement of the print head. The X- and Y-axes operate at a controlled speed of 0.2 mm/s, while the Z axis moves upward by 0.1 mm after each printed layer. The printhead employs a syringe mechanism, this design modifies a conventional polypropylene syringe by introducing coaxial holes in both the plunger and the push rod, allowing direct insertion of the working electrode into the electrolyte. The electrode is tightly fitted into the plunger hole, creating an interference seal with the rubber piston material to prevent leakage. Importantly, the syringe body and actuation mechanism are structurally decoupled from the electrode holder, ensuring that mechanical forces from piston movement do not disturb the electrode position. This configuration enables precise control of electrolyte flow and stable electrochemical deposition. Figure 1 shows the schematic diagram of the ECAM device.

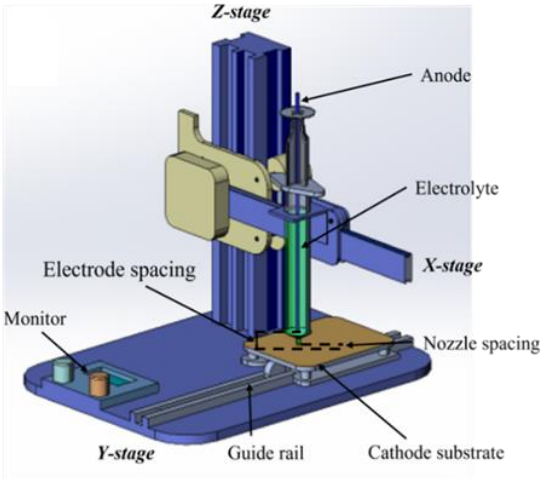

Figure 1. Schematic diagram of ECAM device.

Figure 2 illustrates the working principle of ECAM process, which relies on localized meniscus-confined electrochemical deposition. In this process, the nozzle had an outer diameter of 0.5 mm and an inner diameter of 0.4 mm. The nozzle filled with $CuSO_4$-based electrolyte was positioned in close proximity to the conductive substrate. A stable meniscus naturally forms between the nozzle tip and the substrate due to surface tension and capillary effects. The nozzle-to-substrate distance was initially set to 0.1 mm using a precision leveling mechanism, allowing for the formation of a well-confined meniscus that ensures

localized and controlled deposition. Under an applied electric field, copper ions in the electrolyte are reduced and deposited onto the substrate through controlled electrochemical reactions [22]. The primary reactions are involved as follows:

Cu^{2+} in the electrolyte gain electrons and are reduced to metallic copper, which is deposited onto the substrate to form the printed parts. Under certain conditions, hydrogen evolution may also occur as a side reaction:

$$2H^{+} + 2e^{-} \rightarrow H_2 \uparrow \quad (1)$$

H^{+} may also be reduced, producing hydrogen gas as a side reaction, particularly under high overpotential conditions.

Anode (copper):

$$Cu(s) \rightarrow Cu^{2+} + 2e^{-} \quad (2)$$

Copper atoms at the anode are oxidized into Cu^{2+} ions, which replenish the electrolyte and maintain charge neutrality. In the schematic illustration, Cu^{2+} (represented as green dots) migrate downward through the confined meniscus and are reduced at the cathode, while electrons flow from the external power supply through the conductive substrate. The overall process enables localized, directional, and high-resolution electrodeposition of copper structures under a controlled electric field [23].

The meniscus plays a critical role in confining the electrolyte and maintaining deposition resolution. Its shape and pressure balance are governed by the Young–Laplace equation:

$$\Delta P = \gamma \left(\frac{1}{R_1} + \frac{1}{R_2} \right) \quad (3)$$

where ΔP is the pressure difference across the liquid interface, γ is the surface tension, and R_1, R_2 are the principal curvature radii of the meniscus. The flow and replenishment of electrolyte inside the meniscus is driven by capillary action and can be approximated by the Washburn equation:

$$L(t) = \sqrt{\left[\frac{\gamma R \cos\theta}{2\mu} \right] t} \quad (4)$$

where L(t) is the penetration depth, R is the capillary radius, θ is the contact angle, μ is the viscosity, and t is time. These principles jointly ensure electrolyte supply and electrochemical confinement during localized copper deposition.

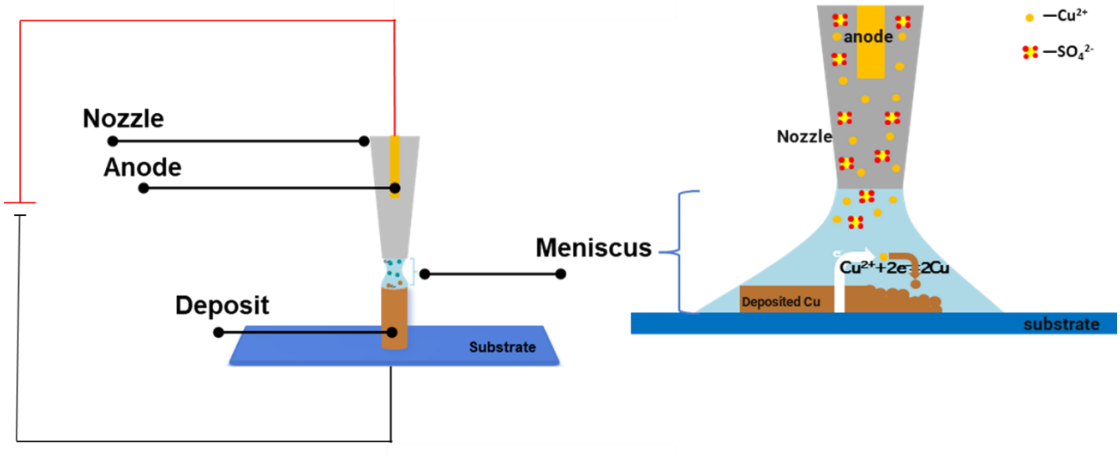

Figure 2. Electrochemical additive manufacturing (ECAM) processes.

For the complex-shaped copper printing, the study attempted the printing of Single-point copper (Figure 3), the “L”-shaped letter (Figure 4a), and a circular copper component (Figure 4b). Figure 3 shows a schematic diagram of single-point printing. In Figure 3a, the stage moves close to the substrate preparing for printing. In Figure 3b, a meniscus is formed between the nozzle and the substrate, where printing takes place to build the copper pillar upwards. Figure 3c illustrates the ECAM process during which copper is deposited through the meniscus. Finally, Figure 3d shows the stage moving away after printing is complete. The single-point printing of copper part (Figure 3) was performed using 1 M $CuSO_4$ solution with and without the addition of NaCl at applied voltages of 5 V, 10 V, and 30 V respectively, to compare the printing rates at different voltages and to evaluate the effect of NaCl on printing rate of the parts.

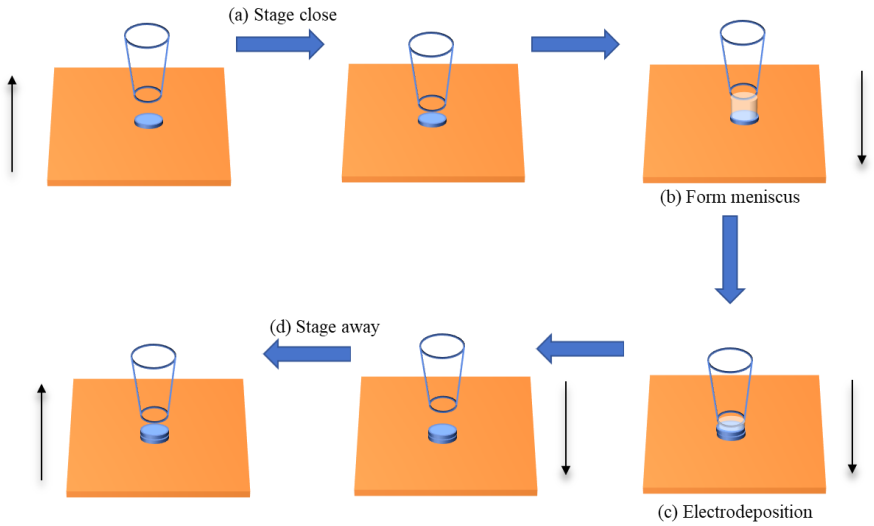

Figure 3. Schematic diagram of single-point deposition. **(a)** Stage close; **(b)** Form meniscus; **(c)** ECAM process; **(d)** Stage away.

Figure 4 shows the printing path of the nozzle and layer distribution for the “L”-shaped structure part (Figure 4a) and the circular copper component (Figure 4b). Both structures were printed at 5 V for 2 hours, with a nozzle movement speed of 0.4 mm/s and a layer height of 0.01 mm. The “L”-shaped structure comprised 30 layers, while the circular component consisted of 40 layers.

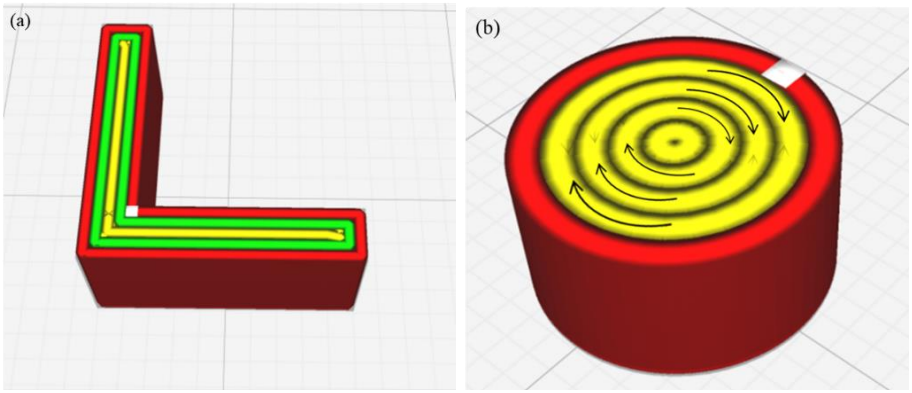

Figure 4. Copper printing path and layer distribution diagram: **(a)** “L”-shaped letter; **(b)** Circular copper component.

In addition to the printing of single-point deposits, L-shaped structures, and circular components, linear copper structures were also fabricated to systematically investigate the effects of process parameters. These linear structure pasts were printed on the basis of single-point deposition at an optimized deposition voltage of 3 V. The experiments focused on evaluating the influence of different feed rates, nozzle-to-substrate spacings, and electrode-to-substrate spacings. For all linear depositions, the printing time was fixed at 2 h, with a layer height of 0.01 mm and 35 layers.

2.2. Preparation procedure of MCED

Before preparing the sample, the copper plate was polished sequentially with 800, 1000, and 1600 mesh metallographic sandpapers to remove the surface oxide layer. It was then cleaned in an ultrasonic cleaner for 30 minutes to eliminate surface impurities and oil residues. Afterward, the plate was rinsed with 20% dilute hydrochloric acid to activate the surface, followed by thorough rinsing with deionized water and drying. 1 M $CuSO_4$ solution was stirred and heated on a magnetic stirrer, and the pH was measured using a pH meter. The pH was adjusted with 20% dilute sulfuric acid to reach the desired value. The final solution parameters are listed in Table 1 NaCl was added to the $CuSO_4$ solution to enhance the conductivity of the electrolyte, thereby facilitating electrochemical deposition. The prepared $CuSO_4$ solution was loaded into a modified syringe, and a pure copper anode (99.99%) wire with a diameter of 0.4 mm and a length of 300 mm was inserted through the hole in the rubber piston and pushed in solution using the pusher rod. Electrical connections were established by linking the copper anode and the cathode substrate to the power supply's positive and negative terminals, respectively, and the deposition voltage was adjusted as required. The 3D model of the desired structure was imported into Cura software, which was used to control the movement of the print nozzle to the substrate. The nozzle-to-substrate distance was adjusted to 0.1 mm using the leveling screw located at the base of the substrate holder. For printing circular parts, a stainless-steel plate was used as the substrate instead of the copper plate. After ECAM process, the sample was cut from the plate using a cutting machine. The surface of the sample was first wiped with alcohol, followed by ultrasonic cleaning for 30 minutes. Finally, the sample was dried.

Table 1. Bath chemistry of the $CuSO_4$ electrolyte and the printing parameters.

Process parameters	Value
$CuSO_4 \cdot 5H_2O$ (mol/L)	1
NaCl (g/L)	10
pH	4.5
Electrical conductivity/(ms/cm)	6.25*/15
Temperature/°C	20
Applied voltage/V	5–30

Note: The value is taken from the electrolyte without the addition of NaCl.

2.3. Characterizations

The microstructure and morphology of the surface of the printed deposits were analyzed by a digital optical microscope (OM, VHX-700FC) and scanning electron microscopy (SEM, su1510/EVO18/Sigma 500). In addition, a two-dimensional electrochemical simulation was performed using COMSOL Multiphysics

to investigate the electric field distribution at different nozzle-to-substrate and electrode spacings, providing insights into the deposition behavior and meniscus stability.

3. Results

Figure 5 illustrates the macro-morphological appearance of copper pillars deposited under different voltages and electrolyte conditions. Figure 5a shows the morphology of copper pillars deposited at 5 V in a NaCl-containing solution. Under this condition, the pillars appear relatively short and uniform, with a compact and dense surface. The lower deposition voltage effectively suppresses the growth kinetics, resulting in reduced dendritic formation and improved structural regularity. In contrast, increasing the voltage to 10 V in the same NaCl-containing electrolyte leads to rougher and more open structures, as shown in Figure 5b. Figures 5(b1–b3) present enlarged views of the upper (Figure 5(b1)), middle (Figure 5(b2)), and lower regions (Figure 5(b3)) of the pillar in Figure 5b, respectively. Dendritic features are evident throughout the entire pillar, becoming increasingly pronounced and disordered along the vertical axis, reflecting unstable growth behavior. Meanwhile, deposition at 10 V in a NaCl-free solution (Figure 5c) also results in dendritic structures, but the overall surface appears denser and more compact compared to Figure 5b. When the voltage is further increased to 30 V in the NaCl-free solution (Figure 5d), the pillar exhibits severe dendritic overgrowth and surface burning, indicating instability caused by excessive current density and localized heating. These observations demonstrate that both the applied voltage and the electrolyte composition significantly affect the morphology and integrity of the deposited copper structures.

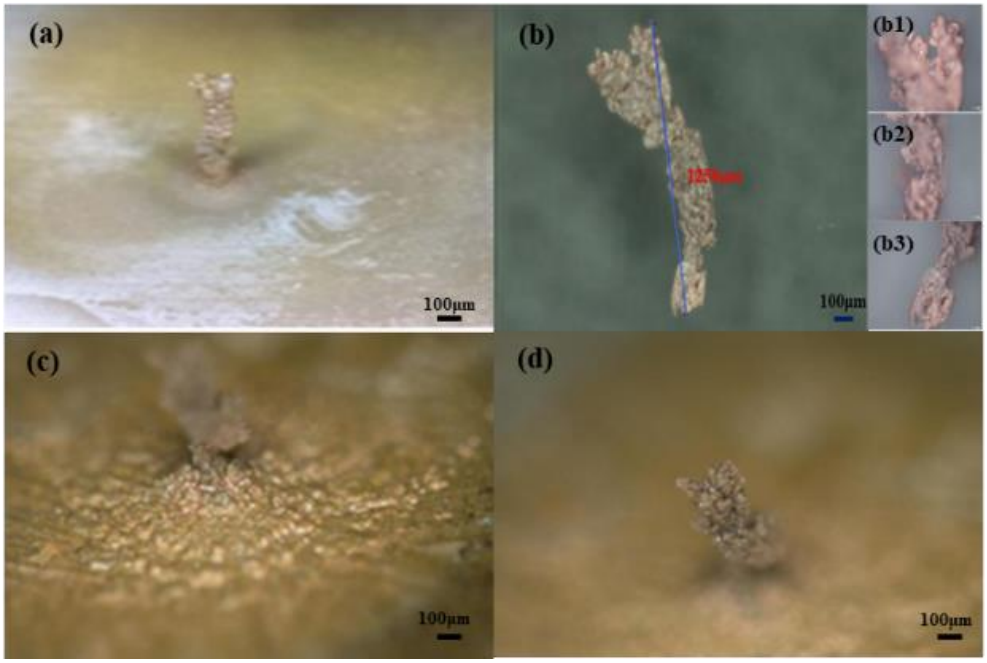

Figure 5. Optical micrographs of the copper pillar deposited under different voltage and electrolyte conditions **(a)** Applied voltage of 5 V and **(b)** 10V in solution with the addition of NaCl; **(c)** applied voltage of 10 V and **(d)** 30 V in solution with the absence of NaCl; **(b1–b3)** Enlarged views of different regions of the pillar shown in **(b)**, highlighting the porous and dendritic features in greater detail.

Figure 6 provides close-up optical images of the base region of copper pillars printed at 10.0 V, offering insights into the initial growth behavior under different electrolyte conditions. In Figure 6a, for the solution without the presence of NaCl, the base exhibits a circular and relatively uniform shape, indicating symmetrical ion transport and stable deposition. In contrast, for the solution with addition of NaCl (Figure 6b), a petal-like radial pattern is present, suggesting anisotropic growth caused by variations in local current density. This morphological difference is likely due to the enhanced ionic conductivity introduced by NaCl, which alters the electric field distribution at the nozzle–substrate interface and promotes outward-directed growth during the early deposition phase. Additionally, both bases are wider than the final pillar diameter, indicating that deposition initially spreads laterally before becoming vertically confined as the structure grows upward [20].

Deposition conditions and corresponding results are summarized in Table 2. As the applied voltage increases, the electrochemical driving force is enhanced, thereby accelerating the deposition process [10]. In addition, the incorporation of NaCl further promotes deposition by improving the electrolyte conductivity. Notably, the combined effect of high voltage and a NaCl-containing solution significantly enhances the deposition rate. However, excessively rapid deposition—especially when associated with dendritic growth—can negatively impact the structural precision and mechanical robustness of the printed features. Therefore, although this approach improves efficiency, a careful balance between deposition speed and structural quality is essential for practical applications.

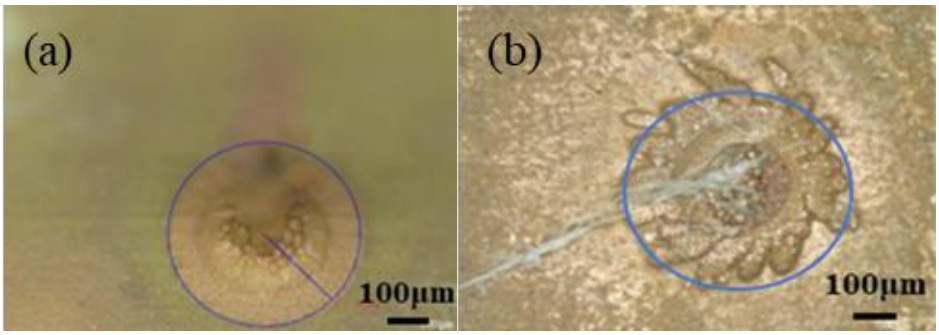

Figure 6. Optical images of the bottom features of copper pillars fabricated by ECAM: **(a)** Applied voltage of 10 V in solution without the addition of NaCl; **(b)** applied voltage of 10V in solution with the addition of NaCl.

Table 2. Time required for copper printing under various process parameters.

Solution	Concentration (mol/L)	Electrical conductivity (ms/cm)	Voltage (V)	Time (min)
$CuSO_4$ + 10g/L NaCl	1	15	10	10
$CuSO_4$ + 10g/L NaCl	1	15	5	20
$CuSO_4$	1	6.25	10	32
$CuSO_4$	1	6.25	30	10

Based on single-point printing, line-shaped copper components were printed at an optimized printing voltage of 3 V. To investigate the influence of process parameters on the geometry and quality

of the printed features, different feed rates, nozzle-to-substrate spacings, and electrode spacings were applied. The corresponding results are shown in Figures 7–9 and Tables 3–5.

Figure 7 presents the optical images of line-shaped copper components printed at varying nozzle feed rates, with corresponding width data summarized in Table 3 The results clearly show that the printed parts exhibit the greatest inner and outer widths at a feed rate of 0.4 mm/s (Figure 7b), with values of 2.14 mm and 3.61 mm, respectively. Beyond this optimal speed, both widths decrease with increasing feed rate, indicating a reduction in material printing. Specifically, at 0.2 mm/s (Figure 7a), the inner width is 1.88 mm and the outer width is 2.73 mm. At 0.6 mm/s (Figure 7c), the inner width is 1.82 mm and the outer width is 3.02 mm. As the feed rate increased to 1 mm/s (Figure 7d), the inner width is 1.63 mm and the outer width is 2.97 mm. The optimal performance at a feed rate of 0.4 mm/s (Figure 7b) can be attributed to a balance between electrolyte replenishment and printing kinetics. At this speed, sufficient Cu^{2+} are delivered to the cathode surface, enabling steady nucleation and compact growth. This behavior aligns with the Washburn Equation (4), which describes capillary-driven flow within the meniscus. When the nozzle moves too fast, ion transport cannot keep pace with the electrochemical reduction, leading to incomplete coverage and widened gaps between grains [23]. Conversely, slower rates increase ion residence time, which may cause supersaturation and uncontrolled lateral spreading, degrading structural uniformity. Figures 7(a1–d1) further illustrate these trends, providing magnified views of the printed lines shown in Figures 7a–d under optical microscopy. At 0.2 mm/s (Figure 7(a1)), the grains are evenly distributed, but the line width is relatively small. At 0.4 mm/s (Figure 7(b1)), copper grains are more evenly distributed with minimal spacing. At 0.6 mm/s (Figure 7(c1)) and 1 mm/s (Figure 7(d1)), the surface of the printed line-part becomes porous due to limited ion transport. In summary, the feed rate of 0.4 mm/s represents an optimal condition where meniscus stability, ion diffusion, and printing rate are well-coordinated, resulting in dense, uniform line-shaped copper components with minimal defects.

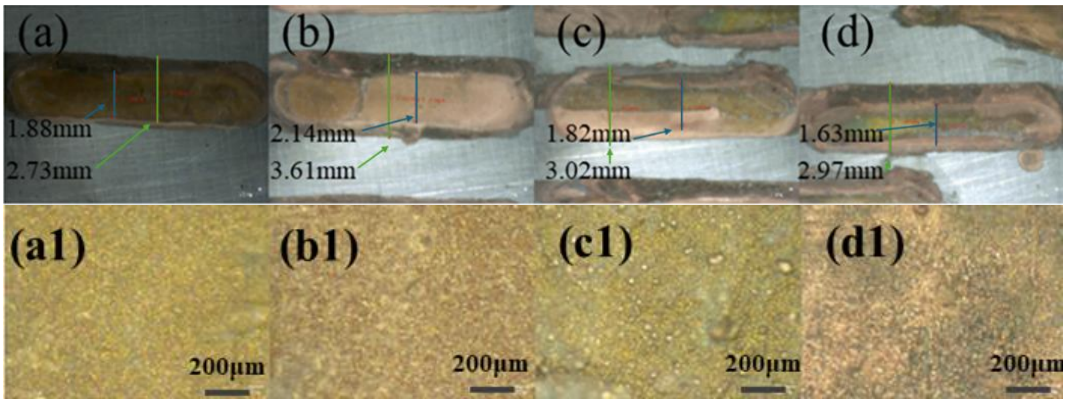

Figure 7. Optical images of copper lines printing at different feed rates **(a)** and **(a1)** 0.2 mm/s; **(b)** and **(b1)** 0.4 mm/s; **(c)** and **(c1)** 0.6 mm/s; **(d)** and **(d1)** 1 mm/s.

Figure 8 presents optical images of copper lines printed at different nozzle spacings. According to the data in Figure 8 and Table 4, the outer width of the printed copper line is greatest at a nozzle spacing of 0.1 mm (Figure 8a) and smallest at 0.3 mm (Figure 8b), while the inner width is also largest at 0.1 mm and smallest at 1 mm spacing (Figure 8c). Overall, the width of the printed copper line decreases as the nozzle spacing increases, with the widest line formed at 0.1 mm and the narrowest at 1 mm spacing. This trend is attributed to the influence of nozzle spacing on the meniscus size. A smaller spacing resulted in a larger and more stable meniscus, which expands the effective printing area. Whereas

larger spacing reduces meniscus size and thus narrows the printed line-shaped parts. As a result, the size of the printed structure decreases with increasing nozzle spacing, potentially improving printing accuracy. Figures 8(a1–c1) further illustrate these trends, providing magnified views of the printed line-shaped parts shown in Figures 8a–c under optical microscopy. The line-shaped copper components printed at smaller nozzle spacings (Figure 8(a1)) exhibit smoother surfaces and more uniform crystal structures, while those printed at larger spacings (Figures 8(b1,c1)) show rougher and more irregular morphologies. This indicates that increasing the nozzle spacing reduces the local current density between the substrate and the nozzle, thereby decreasing both the deposition rate and structural uniformity. These observations are consistent with the theoretical analysis based on the Young–Laplace Equation (3), which describes meniscus curvature and stability. Smaller nozzle spacing enhances confinement and stability of the meniscus, promoting uniform line formation, whereas larger spacing increases instability, resulting in less uniform line-shaped copper components.

Table 3. Width of line-shaped copper components printed at various feed rates.

Width (mm)	0.2 mm/s	0.4 mm/s	0.6 mm/s	1 mm/s
Inner width	1.88	2.14	1.82	1.63
Outer width	2.73	3.61	3.02	2.97

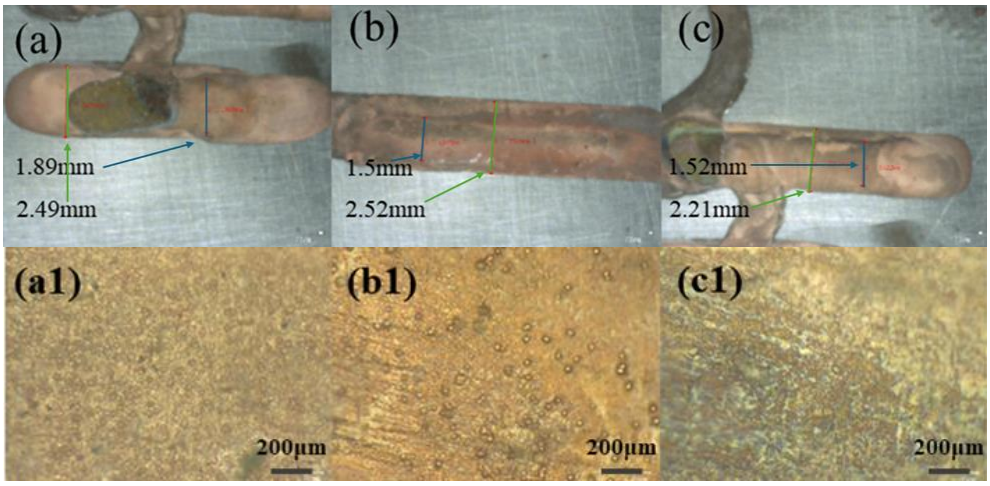

Figure 8. Optical micrographs of line-shaped copper components printed at various nozzle spacings **(a)** and **(a1)** 0.1 mm; **(b)** and **(b1)** 0.3 mm; **(c)** and **(c1)** 1 mm.

Table 4. Width of copper lines printed at various nozzle spacings.

Width (mm)	0.1 mm	0.3 mm	1 mm
Inner width	1.89	1.5	1.52
Outer width	2.49	2.52	2.21

Figure 9 shows optical images of copper wires printed at different electrode spacings. According to the analysis of Figure 9 and Table 5, the outer width of the printed copper wire is largest at an electrode spacing of 0.1 mm (Figure 9a) and smallest at 0.3 mm (Figure 9b), while the inner width is greatest at 0.3 mm spacing and smallest at 0.1 mm spacing. Overall, the total width of the copper wire reaches its maximum at 0.3 mm and minimum at 0.1 mm electrode spacing. As the electrode spacing increases, the

inner width of the printed copper wire increases, but the outer width decreases. This behavior is attributed to the effect of electrode spacing on current density at the meniscus. A smaller electrode spacing enhances the current density, accelerating the printing rate particularly in the central region of the wire. In contrast, the current near the edges weakens at larger electrode spacings, reducing the outer width of the wire. From the magnified images (Figures 9(a1,b1)), it is evident that copper wires printed at smaller electrode spacings (Figure 9(a1)) have a more uniform and compact surface morphology compared to those printed at larger spacings (Figure 9(b1)), which show a more uneven distribution of copper particles. This suggests that reducing electrode spacing improves printing accuracy. However, as shown in Figures 9(a) and (a1), copper wires printed at the smallest electrode spacing of 0.1 mm exhibit a burning phenomenon at the center. This is due to excessively high local current density, which causes overheating and leads to the formation of black oxide deposits, as previously reported [22]. The data in Figure 9 and Table 5 indicate that an electrode spacing of 0.3 mm provides an optimal balance by ensuring sufficient ion delivery to the center of the meniscus while avoiding overheating and burning. Conversely, too small a spacing (0.1 mm) raises current density to destabilizing levels, causing meniscus collapse and burning, consistent with predictions from the Young–Laplace Equation (3).

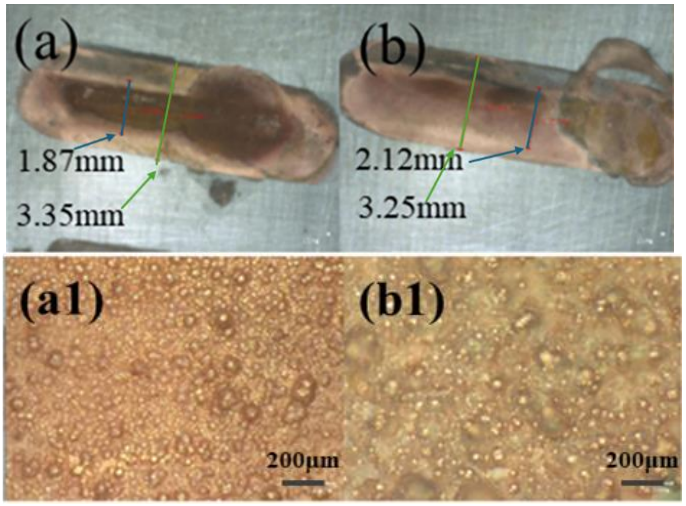

Figure 9. Optical images of line-shaped copper components printing at different electrode spacing **(a)** and **(a1)** 0.1 mm; **(b)** and **(b1)** 0.3 mm.

Table 5. Widths of line-shaped copper components printed at different electrode spacing.

Width (mm)	0.1 mm	0.3 mm
Inner width	1.87	2.12
Outer width	3.35	3.25

The fluctuations in thickness during the printing process led to instability of the meniscus, resulting in uneven printing. This phenomenon is also confirmed in our line-shaped printing experiments, where the printed parts exhibit dimensional inconsistencies in the horizontal direction. Specifically, clear differences between the inner and outer widths are observed, manifesting as a characteristic 'coffee ring' effect [23]. These findings collectively indicate that precise control of movement speed, nozzle gap, and electrode spacing is critical for achieving high geometrical accuracy in ECAM. Optimal settings such as

a feed rate of 0.4 mm/s, nozzle distance of 0.1 mm, and electrode gap of 0.3 mm can minimize dimensional deviations and improve the fidelity of printed copper structures.

Figure 10 presents the 2D and 3D optical micrographs of a printed "L"-shaped copper structure. The printing was performed at the voltage of 5 V for 2 hours, using a movement speed of 0.4 mm/s and a 0.4 mm diameter nozzle. The deposition was carried out on a mechanically polished copper substrate with visible surface roughness. As shown in Figure 10a, some fine scratches can still be observed on the substrate surface, providing contrast with the printed region. Figure 10b provides a magnified view of the local surface morphology, where the printed structure appears dense and compact under these conditions. The 3D optical image in Figure 10c reveals a rough surface texture with noticeable ridges and valleys, indicating significant topographical variation across the printed layers. The maximum height difference measured in the printed region is approximately 36.12 μm, reflecting the vertical growth and surface undulation of the deposited copper.

Figure 11 shows the optical and SEM images of round copper elements fabricated under the same voltage and printing time but using a 2 mm diameter nozzle. The printing was conducted on a polished steel substrate. Figure 11a displays a macroscopic image of the printed circular part directly beneath the nozzle, showing a dense and uniform copper deposit. Figure 11b presents a 2D optical micrograph of the printed region, where the surface appears compact and continuous. However, slight discoloration in some areas is observed, likely due to oxidation from exposure to air. The SEM image in Figure 11c reveals a relatively smooth and flat surface morphology at low magnification, indicating uniform layer formation during deposition. In contrast, the high-magnification SEM image in Figure 11d shows localized protrusions and fine surface scratches. These features may result from slight surface irregularities of the steel substrate or inhomogeneous nucleation during the early stage of deposition. Overall, the printed copper element maintains good surface integrity, demonstrating the feasibility of printing on steel substrates with larger nozzle sizes.

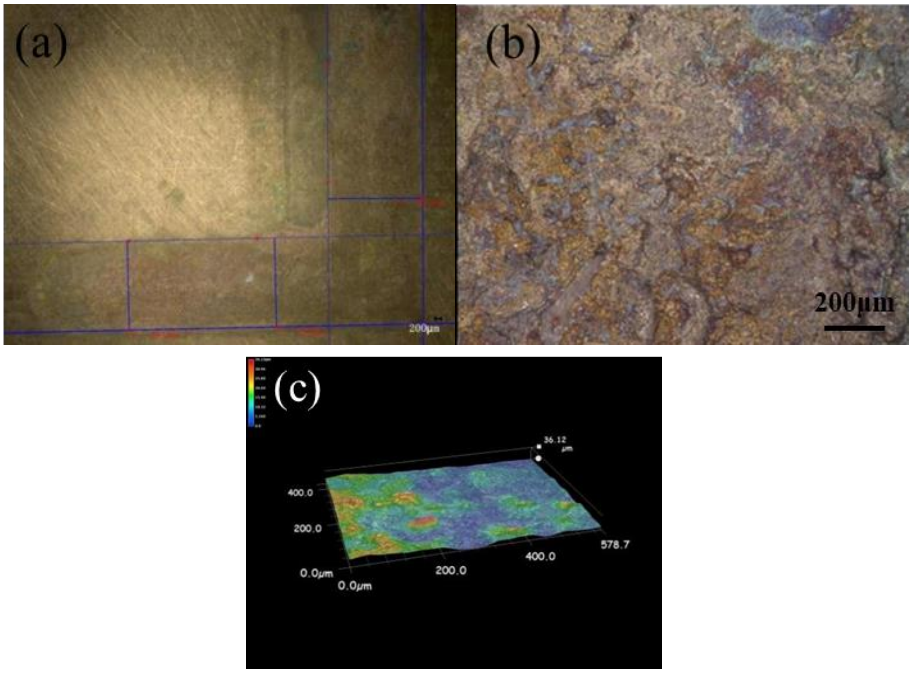

Figure 10. OM 2D and 3D micrographs of the 'L'-shaped copper component **(a)** Macroscopic overview; **(b)** Detailed local view; **(c)** 3D optical microscopy morphology.

Between the "L"-shaped and round copper parts indicates that the round structures, printed with the 2 mm diameter nozzle, exhibit better surface smoothness and uniformity. In contrast, the "L"-shaped part fabricated with a 0.4 mm sponge-filled nozzle displays more pronounced dimensional variation at the edges. This difference can be attributed to two primary factors. First, the "L"-shaped structure was printed on a rough copper substrate, whereas the round component was printed on a smooth steel substrate. The rough substrate may have caused local variations in current density during printing process, negatively impacting the uniformity of the parts. Second, the sponge-filled nozzle used for the "L"-shaped part provided less precise meniscus control compared to the purpose-designed nozzle used for the round part. This led to occasional leakage and exacerbated the "coffee-ring" effect, resulting in both horizontal and vertical printing fluctuations. Consequently, the overall dimensional accuracy of the printed part was reduced.

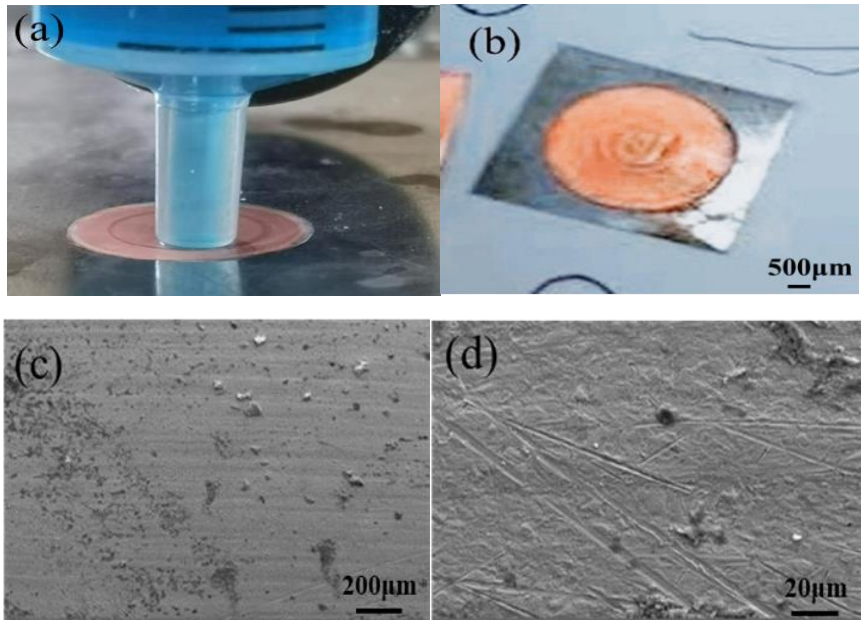

Figure 11. Optical and SEM images of round copper elements on the steel substrates **(a)** Printing macrograph; **(b)** 2D optical micrograph, SEM images with low magnification; **(c)** and high magnification; **(d)** Comparative analysis.

4. Discussion

Figure 12 shows the current–time (I–T) curves of copper printing at different applied voltages ranging from 2 V to 10 V. The measurements were performed using a two-electrode setup on an electrochemical workstation, with Ag/AgCl/3M KCl as the reference electrode. As the voltage increases, the overall current level rises, reflecting enhanced electrochemical driving force and ion migration. Figure 12 presents the current–time (I–T) curves of copper printing under constant voltages ranging from 2 V to 10 V. The current response generally increases with voltage, but the trend is nonlinear and exhibits several transient features. At low voltages of 2–4 V, the current is relatively stable but low, reflecting limited driving force for Cu^{2+} reduction and slower printing kinetics. As the printing voltage increases to 5–7 V, the current rises and becomes more stable, suggesting improved ion migration and charge transfer. However, at the applied voltage of 6 V, a gradual decline in current is observed, likely due to ion depletion in the localized electrolyte zone or accumulation of byproducts at the electrode interface. At higher voltages

of 8–10 V, transient fluctuations and abrupt current drops become more prominent. These are attributed to gas evolution (e.g., hydrogen), meniscus instability, or electrolyte disturbance near the nozzle tip. Notably, the current at 10 V terminates earlier (around 440 s), indicating potential drying of the nozzle or local electrolyte exhaustion. These experimental observations are consistent with previous modeling work by Brant and Sundaram [12], who employed molecular dynamics simulations to study nanoscale overpotential-driven printing in ECAM systems. Their results demonstrated that although increasing voltage can enhance initial printing, it also promotes central ion depletion and destabilizes the current once a critical overpotential is exceeded. This behavior aligns well with theoretical predictions based on the Young–Laplace Equation (3), which describes how increased pressure and instability at the meniscus can affect printing dynamics under high voltage conditions. Based on the current–time analysis, an applied voltage of 3 V was selected for line-shaped copper printing, as it provides a stable and moderate current suitable for precise, uniform one-dimensional printing, minimizing meniscus instability and side reactions. For the printing of more complex geometries such as L-shaped and circular structures, a slightly higher voltage of 5 V was chosen. This higher voltage ensures sufficient ion supply and printing rate during path redirection and curvature transitions, enabling smoother growth along multidirectional trajectories without significant current drop or structural discontinuity. These voltage settings were optimized to balance printing stability and structural fidelity in both simple and complex ECAM printing.

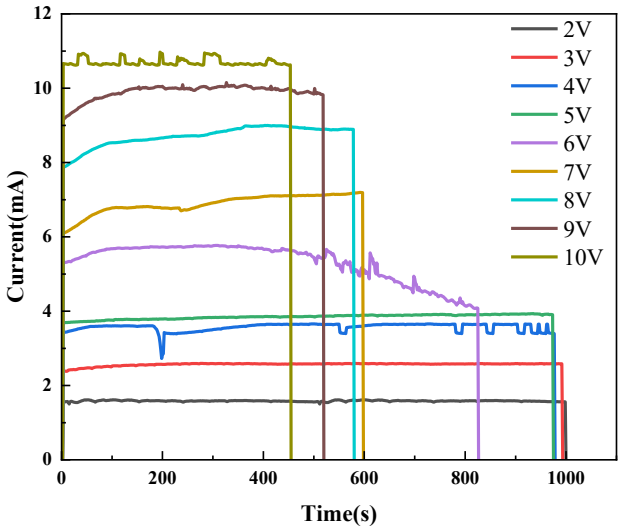

Figure 12. Current–time (I–T) curves of copper printing at different applied voltages.

Figure 13 illustrates the effects of electrolyte composition and applied voltage on the printing time of copper pillars. As shown in Figure 13 and supported by the data in Table 2, the printing duration of copper pillars is strongly influenced by electrolyte composition and applied voltage. The addition of 10 g/L NaCl to the $CuSO_4$ solution increases the electrolyte conductivity from 6.25 mS/cm to 15 mS/cm, which significantly enhances the deposition rate. For example, at the voltage of 10 V, the printing time decreases sharply from 32 minutes without NaCl to 10 minutes with NaCl, demonstrating how improved ionic conductivity accelerates the deposition rate by promoting faster ion transport and improving printing efficiency. Conversely, at a lower voltage of 5 V, even with NaCl-enhanced conductivity, the printing time increases to 20 minutes, indicating that a minimum electrochemical driving force is still necessary to sustain efficient Cu^{2+} reduction. Similarly, applying a higher voltage of 30 V in a low-conductivity electrolyte without the addition of NaCl also achieves a 10-minute printing time, but

this approach may introduce side effects such as local overheating or meniscus instability, as noted earlier. Therefore, the data in Table 2 validate the trends observed in Figure 13, confirming that both higher voltage and higher ionic conductivity contribute to faster copper printing. However, the combination of moderate voltage (10 V) with improved conductivity (via NaCl addition) offers a more stable and efficient condition for pillar formation, avoiding the risks associated with extreme voltage conditions. This further supports the notion that optimizing electrolyte formulation is as crucial as voltage selection in ECAM processes.

Figure 14 provides a schematic representation of the meniscus morphology during the ECAM printing process. Figure 14a presents a front view of the meniscus during deposition, highlighting the Young–Laplace pressure difference (ΔP), principal curvature radii (R1 and R2), and contact angle (θ) between the electrolyte and the substrate. The meniscus is confined between the nozzle and the substrate due to surface tension, and its curvature governs the local pressure and electrolyte confinement, which in turn influence deposition uniformity. Figure 14b shows a side view of the dynamic meniscus during nozzle movement, where fluctuations in meniscus shape occur due to the interplay between fluid flow, capillary action, and nozzle translation. These dynamic instabilities of the meniscus are directly linked to the thickness variations observed in our printed copper structures. As the nozzle moves, any perturbation in meniscus stability can lead to inconsistent ion flux and uneven deposition, resulting in printed lines with non-uniform cross-sections. This is consistent with the printing results of the experimental observations in line-shaped copper parts, where dimensional inconsistencies are evident in both horizontal and vertical directions. Specifically, we observed varying diameters along the height of the deposited structures and irregular widths across horizontal layers, which collectively exhibit a characteristic “coffee ring” effect [23]. Such phenomena arise from local accumulation and depletion of ions at the advancing meniscus edge, as well as asymmetric drying and flow patterns within the confined electrolyte region. These findings underscore the critical importance of maintaining a stable meniscus profile during printing. The geometrical shape and curvature of the meniscus, as modeled by the Young–Laplace Equation (3), are essential for ensuring controlled deposition and consistent feature geometry. Moreover, this analysis highlights the necessity of optimizing process parameters, including feed rate, nozzle-substrate distance, and electrode spacing, not only to improve deposition fidelity but also to suppress meniscus instabilities that may otherwise compromise the quality of printed parts.

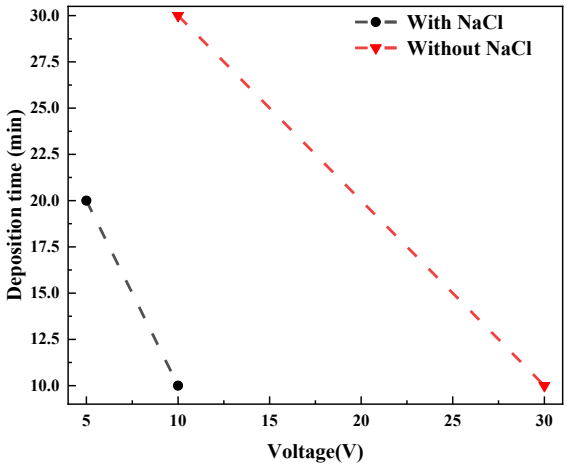

Figure 13. Printing time of copper pillars under different electrolyte compositions and voltages (the solution with and without the addition of NaCl).

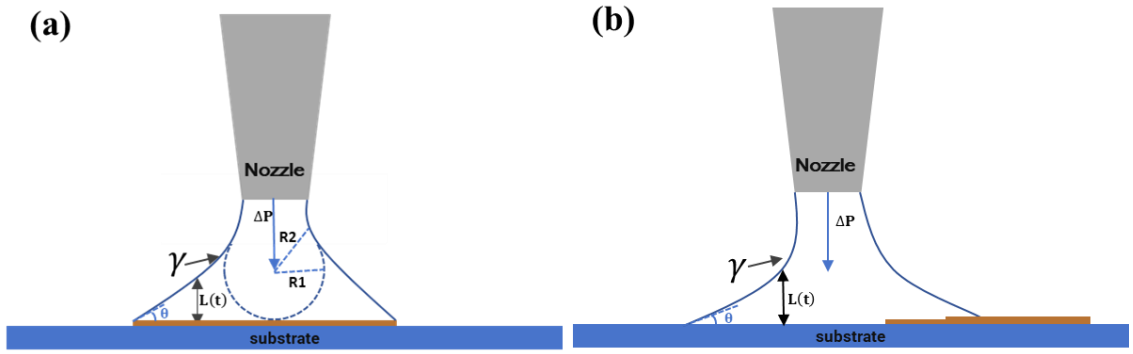

Figure 14. Schematic illustration of the meniscus during the printing process **(a)** front view; **(b)** side view during nozzle movement.

Figure 15 shows the COMSOL simulation of the electric field distribution at different nozzle-to-substrate and electrode spacings. Figure 15a presents the overall simulation domain, Figure 15b provides a close-up view of the region between the nozzle and cathode, and Figures 15c–e shows detailed views of the meniscus area under varied parameter conditions. The electric field lines are concentrated and uniform near the nozzle tip but begin to diverge at the meniscus, spreading from the center toward the edges and becoming sparser farther from the center. The field lines also incline from the cathode substrate toward the anode, which slows deposition at the meniscus edges, causing uneven deposition. The central region of concentrated and non-divergent electric field corresponds approximately to half the size of the overall deposition spot. This electric field distribution is consistent with the experimental observations in Section 3 regarding linear copper deposition. As shown in Figure 8 and Table 4, smaller nozzle spacings (e.g., 0.1 mm) result in larger menisci and wider deposited copper lines due to stronger, more confined electric fields. The simulation (Figure 15d) confirms that reduced nozzle spacing produces denser and less divergent electric field lines at the meniscus center, supporting a wider and more uniform deposition region. Conversely, larger nozzle spacing (e.g., 1 mm) enlarges the meniscus but leads to more divergent and sparser electric field lines (Figure 15c), corresponding experimentally to narrower lines with coarser and less uniform morphology. Similarly, the influence of electrode spacing is reflected in both simulation and experiments. Figure 9 and Table 5 demonstrate that smaller electrode spacing (0.1 mm) increases current density at the meniscus center, accelerating deposition but risking overheating and burning due to excessive local current density. The COMSOL simulation (Figure 15e) reveals that reduced electrode spacing concentrates electric field lines more densely at the meniscus center but also intensifies divergence at the edges, which can cause uneven deposition and meniscus instability. An optimal electrode spacing (0.3 mm) balances sufficient central current density and mitigates edge divergence, matching the observed improved deposition uniformity and avoidance of burning. Moreover, the feed rate effects observed experimentally (Figure 7) align indirectly with these electric field distributions. An optimal feed rate (0.4 mm/s) ensures balanced ion supply and reaction kinetics, which, when coupled with favorable electric field distributions at the meniscus, results in uniform nucleation and compact growth. Excessively fast or slow feed rates disturb this balance, aggravating porosity or disordered growth due to mismatched ion transport relative to deposition rate, a phenomenon indirectly governed by the localized electric field and meniscus shape. In summary, the COMSOL simulations elucidate the spatial variations of electric field intensity and direction at the meniscus, providing a physical basis

for interpreting the effects of nozzle and electrode spacing on deposition morphology and accuracy observed in the experiments. Optimizing these parameters enhances electric field confinement, stabilizes the meniscus, and promotes uniform copper deposition with high geometrical fidelity in the ECAM process.

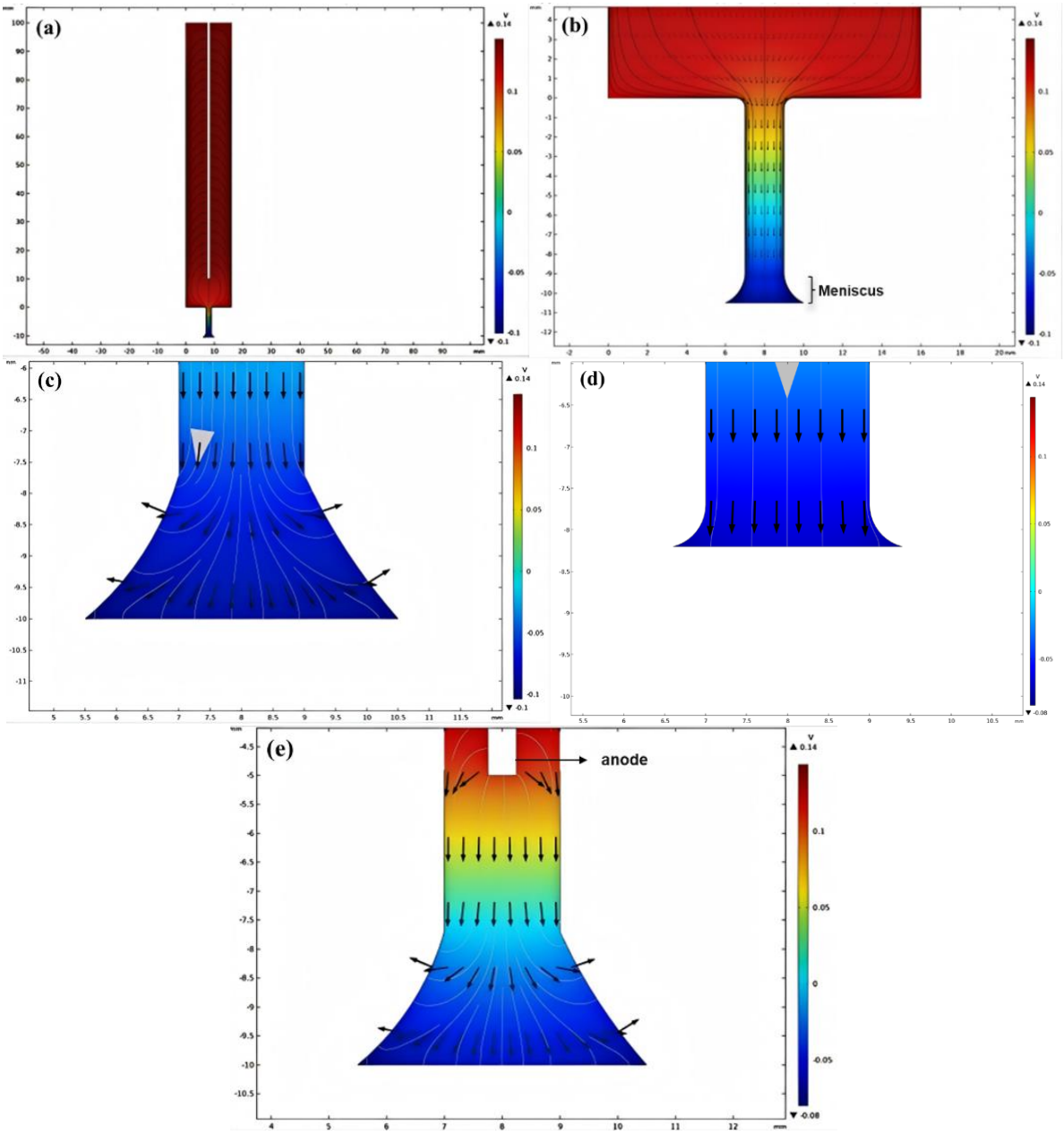

Figure 15. COMSOL simulation of electric field distribution under different nozzle and electrode spacings:**(a)** Overall view of the simulation domain; **(b)** local magnification between nozzle and cathode; **(c)** high nozzle spacing and high electrode spacing; **(d)** low nozzle spacing and high electrode spacing; **(e)** low nozzle spacing and low electrode spacing.

Figure 16 presents the widths of line-shaped copper parts printed under varying process parameters, including feed rate, nozzle-to-substrate spacing, and electrode spacing. On the X-axis, the respective parameter values are plotted, while the Y-axis shows the average line width, calculated as the average of the outer widths, with error bars representing the standard deviation to reflect measurement variability and structural uniformity. As shown in Figure 16a, the average line width increases initially with feed

rate, reaching a maximum at 0.4 mm/s, then decreases at higher speeds. This trend aligns with the underlying deposition mechanisms has been discussed in Section 3, where the feed rate of 0.4 mm/s balances ion supply and deposition kinetics, producing wider and uniform line-shaped copper parts. At lower speeds, ion accumulation causes irregular growth, while faster movement limits ion availability, reducing line width. Figure 16b demonstrates that increasing nozzle-to-substrate spacing leads to a decrease in average line width. Smaller spacing of 0.1 mm results in a larger meniscus and thus wider printed lines, with more uniform surface morphology, while larger spacing reduces meniscus size and current density, narrowing the lines and increasing surface roughness. This behavior is consistent with the meniscus stability predicted by the Young–Laplace Equation (3). In Figure 16c, the average line width varies with electrode spacing, peaking at electrode spacing of 0.1 mm. Small electrode spacing of 0.1 mm generates high local current densities that enhance deposition rate but causes overheating and defects, while large electrode spacing reduces current density and narrows the line. The optimal electrode gap of 0.3 mm achieves uniform deposition with minimized structural defects. The error bars in all three plots indicate consistent reproducibility of the printing process under the given parameters, with relatively low variation near the optimum conditions. In summary, Figure 16 quantitatively confirms that it is essential to precisely control the feed rate, nozzle spacing, and electrode spacing for optimizing line-shaped geometry and quality of the copper parts in ECAM, with the feed rate of 0.4 mm/s, the nozzle spacing of 0.1 mm, and the electrode spacing of 0.3 mm identified as optimal printing parameters.

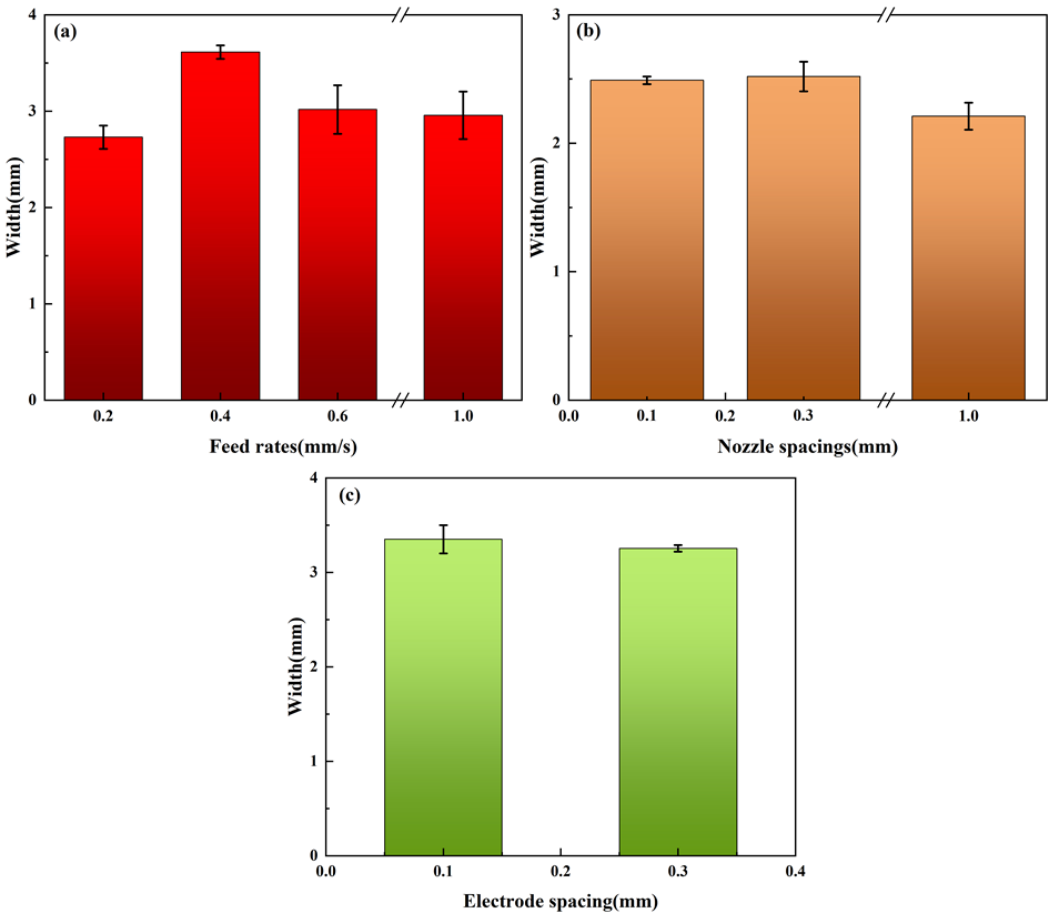

Figure 16. Width of line-shaped copper parts printed under different process parameters. **(a)** Feed rate; **(b)** nozzle spacings; and **(c)** electrode spacing.

5. Conclusions

(1) Under low nozzle spacing and low electrode spacing, the electric field lines in the meniscus area are denser. The current density is higher, the electrolyte concentration is greater, and the printing speed is faster. Printing accuracy is higher with high feed rate, high nozzle spacing, and low electrode spacing; however, high feed rate combined with high nozzle spacing reduces printing quality, and too low electrode spacing can cause burning. The optimized printing parameters are the feed rate of 0.4 mm/s, the lowest possible nozzle spacing of 0.1 mm, and electrode spacing of 0.3 mm.

(2) The higher the printing voltage and the higher the electrolyte concentration, the faster the printing speed. However, a high printing voltage causes dendritic crystal structures to appear in the printed parts, increasing surface roughness and reducing print quality. The best printing quality for copper is achieved at a printing voltage of 3 V.

(3) There is a "coffee ring" effect during the printing process, with fluctuations in the width and height of the printed parts. The initial printed layer of the parts should be larger than the subsequent printed layers, for example, the base outer diameter of the copper pillar should be greater than the diameter of the pillar itself.

In this study, the copper parts were successfully printed by electrochemical additive manufacturing technology, and the printing process parameters were optimized. This work not only provides a theoretical basis and technical support for the additive manufacturing of copper materials, but also offers a reference for electrochemical deposition printing of other metals. Despite these promising results, several challenges remain. Issues such as meniscus instability, local ion depletion, and current-induced burning at low electrode spacing need to be further controlled. Future work should focus on real-time process monitoring, closed-loop control, and multi-material integration. The method shows potential for use in microelectronic interconnects, sensors, and rapid prototyping of conductive features on-demand.

Acknowledgments

Funding: This work was funded by the National Undergraduate Innovation and Entrepreneurship training program innovative training projects (Nos. 201910292022Z, 202010292033Z, 202110292010Z, 202210292024Z).

Conflicts of interests

The authors declare no conflict of interest.

Authors' contribution

X.L.: data curation, writing—original draft, investigation, methodology, visualization, writing—review & editing; W.P.W.: writing—review & editing, supervision, resources, project administration, investigation, conceptualization; Y.A.A.: formal analysis, writing—review & editing, visualization, software, methodology. All authors have read and agreed to the published version of the manuscript.

References

[1] Braun Trevor M, Schwartz Daniel T. The Emerging role of electrodeposition in additive manufacturing. *Electrochem Soc Inte*. 2016, 25(1):69–73.

[2] Chen X, Liu X, Childs P, Brandon N, Wu B. A low cost desktop electrochemical metal 3D printer. *Adv. Mater. Technol.* 2017, 2(10):1700148.

[3] Chen X, Liu X, Ouyang M, Chen J, Taiwo O. Multi-metal 4D printing with a desktop electrochemical 3D printer. *Sci. Rep.* 2019, 9(1):3973.

[4] Hu J, Yu MF. Meniscus-Confined Three-Dimensional Electrodeposition for Direct Writing of Wire Bonds. *Science* 2010, 329 313.

[5] Ayalew AA, Han XL, Suzuki K, Yoshida S, Sakairi M. Fabrication of Ni-microstructure through electrochemical deposition using 3D printed solution flow type microdroplet cell. *Mater. Today Commun.* 2023, 37:107069.

[6] Rajput MS, Pandey PM, Jha S. Micromanufacturing by selective jet electrodeposition process. *Int. J. Adv. Manuf. Technol.* 2015, 76:61–67.

[7] Rajput MS, Pandey PM, Jha S. Modelling of high speed selective jet electrodeposition process. *J. Manuf. Process.* 2015, 17:98–107.

[8] Bilal M, Sakairi M. High throughput electrochemically driven metal microprinting with multicapillary droplet cell. *Mater. Today Commun.* 2021, 26:102053.

[9] Chen YL, Wang Y, Wang Y, Ju BF. Meniscus-confined electrodeposition of metallic microstructures with in-process monitoring of surface qualities. *Precis. Eng.* 2021, 70:34–43.

[10] Wang F, Bian H, Wang F, Sun J, Zhu W. Fabrication of micro copper walls by localized electrochemical deposition through the layer by layer movement of a micro anode. *J. Electrochem. Soc.* 2017, 164(12):758–763.

[11] Han S, Chang P, Zhou Z, Wu Y, Li M. Effect of intermolecular and intramolecular synergism on the inhibition from hybrid additives in damascene copper electrodeposition. *Electrochim. Acta.* 2024, 483:144001.

[12] Brant A, Sundaram M. Molecular dynamics study of direct localized overpotential deposition for nanoscale electrochemical additive manufacturing process. *Precis. Eng.* 2019, 56:412–421.

[13] Morsali S, Daryadel S, Zhou Z, Behroozfar A, Baniasadi M, *et al*. Multi-physics simulation of metal printing at micro/nanoscale using meniscus-confined electrodeposition: Effect of nozzle speed and diameter. *J. Appl. Phys.* 2017, 121(21):203–213.

[14] Sakairi M, Sato F, Gotou Y, Fushimi K, Kikuchi T, *et al*. Development of a novel microstructure fabrication method with co-axial dual capillary solution flow type droplet cells and electrochemical deposition. *Electrochim. Acta.* 2008, 54(2),616–622

[15] Chen X, Liu X, Childs P, Brandon N, Wu B. A low cost desktop electrochemical metal 3D printer. *Adv. Mater. Technol.* 2017, 2:1700148.

[16] Seol S K, Kim D, Lee S, Kim JH, Chang WS, *et al*. Electrodeposition-based 3D Printing of Metallic Microarchitectures with Controlled Internal Structures. *Small* 2015, 11(32):3896–902.

[17] Daryadel S, Behroozfar A, Morsali S R, Moreno S, Baniasadi M, *et al*. Localized Pulsed Electrodeposition Process for Three-Dimensional Printing of Nanotwinned Metallic Nanostructures. *Nano Lett.* 2017, 18:208–214.

[18] Hengsteler J, Mandal B, van Nisselroy C, Lau GPS, Schlotter T, *et al*. Bringing Electrochemical Three-Dimensional printing to the nanoscale. *Nano Lett.* 2021, 21:9093–9101.

[19] Liu P, Guo Y, Wu Y, Chen J, Yang Y. A low-cost electrochemical metal 3D printer based on a microfluidic system for printing mesoscale objects. *Crystals* 2020, 10(4):257.

[20] Hirt L, Ihle S, Pan Z, Dorwling-Carter L, Reiser A, *et al*. Template-Free 3D Microprinting of metals using a force-controlled nanopipette for layer-by-layer electrodeposition. *Adv. Mater.* 2016, 28(12):2311–2315.

[21] Siddiqui H, Singh N, Rao KBS, Kumar S, Chauhan V, *et al*. Meniscus-confined electrochemical additive manufacturing of copper microstructures: Design, fabrication, characterization, and decorative art technology. *Mater. Today Commun.* 2023, 35:105796.

[22] Lei Y, Zhang X, Xu D, Yu M, Yi Z, *et al*. Dynamic “Scanning-Mode” meniscus confined electrodepositing and micropatterning of individually addressable ultraconductive copper line arrays. J. *Phys. Chem. Lett.* 2018, 9(9):2380–2387.

[23] Behroozfar A, Daryadel S, Morsali SR, Moreno S, Baniasadi M, *et al*. Microscale 3D printing of nanotwinned copper. *Adv Mater.* 2018, 30(4):1705107.